frontiers | Frontiers in Remote Sensing

TYPE Original Research
PUBLISHED 20 October 2022
DOI 10.3389/frsen.2022.1009398

Check for updates

OPEN ACCESS

EDITED BY
Carmen Cillero Castro,
3edata Environmental Engineering. S.l., Spain

REVIEWED BY
Richard Zepp,
US Environmental Protection Agency, Athens, United States
Curtis Mobley,
retired from Sequoia Scientific, Inc., United States

*CORRESPONDENCE
Yuting Zhu,
yzhu@syr.edu
Leanne C. Powers,
lcpowers@esf.edu

‡PRESENT ADDRESS
Department of Marine Chemistry and Geochemistry,
Woods Hole Oceanographic Institution,
Woods Hole, MA, United States

†These authors have contributed equally to this work

SPECIALTY SECTION
This article was submitted to Multi- and Hyper-Spectral Imaging, a section of the journal Frontiers in Remote Sensing

RECEIVED 01 August 2022
ACCEPTED 05 October 2022
PUBLISHED 20 October 2022

CITATION
Zhu Y, Powers LC, Kieber DJ and Miller WL (2022), Depth-resolved photochemical production of hydrogen peroxide in the global ocean using remotely sensed ocean color. *Front. Remote Sens.* 3:1009398. doi: 10.3389/frsen.2022.1009398

COPYRIGHT
© 2022 Zhu, Powers, Kieber and Miller. This is an open-access article distributed under the terms of the Creative Commons Attribution License (CC BY). The use, distribution or reproduction in other forums is permitted, provided the original author(s) and the copyright owner(s) are credited and that the original publication in this journal is cited, in accordance with accepted academic practice. No use, distribution or reproduction is permitted which does not comply with these terms.

Depth-resolved photochemical production of hydrogen peroxide in the global ocean using remotely sensed ocean color

Yuting Zhu[1*†‡], Leanne C. Powers[2*†], David J. Kieber[2] and William L. Miller[3]

[1]Wadsworth Center, New York State Department of Health, Albany, NY, United States, [2]Department of Chemistry, State University of New York College of Environmental Science and Forestry, Syracuse, NY, United States, [3]Department of Marine Sciences, University of Georgia, Athens, GA, United States

Hydrogen peroxide (H_2O_2) is an important reactive oxygen species (ROS) in natural waters, affecting water quality *via* participation in metal redox reactions and causing oxidative stress for marine ecosystems. While attempts have been made to better understand H_2O_2 dynamics in the global ocean, the relative importance of various H_2O_2 sources and losses remains uncertain. Our model improves previous estimates of photochemical H_2O_2 production rates by using remotely sensed ocean color to characterize the ultraviolet (UV) radiation field in surface water along with quantitative chemical data for the photochemical efficiency of H_2O_2 formation. Wavelength- and temperature-dependent efficiency (i.e., apparent quantum yield, AQY) spectra previously reported for a variety of seawater sources, including coastal and oligotrophic stations in Antarctica, the Pacific Ocean at Station ALOHA, the Gulf of Mexico, and several sites along the eastern coast of the United States were compiled to obtain a "marine-average" AQY spectrum. To evaluate our predictions of H_2O_2 photoproduction in surface waters using this single AQY spectrum, we compared modeled rates to new measured rates from Gulf Stream, coastal, and nearshore river-outflow stations in the South Atlantic Bight, GA, United States; obtaining comparative differences of 33% or less. In our global model, the "marine-average" AQY spectrum was used with modeled solar irradiance, together with satellite-derived surface seawater temperature and UV optical properties, including diffuse attenuation coefficients and dissolved organic matter absorption coefficients estimated with remote sensing-based algorithms. The final product of the model, a monthly climatology of depth-resolved H_2O_2 photoproduction rates in the surface mixed layer, is reported for the first time and provides an integrated global estimate of ~21.1 Tmol yr^{-1} for photochemical H_2O_2 production. This work has important implications for photo-redox reactions in seawater and improves our understanding of the role of solar irradiation on ROS cycling and the overall oxidation state in the oceans.

KEYWORDS

photochemistry, superoxide, remote sensing, UV radiation, reactive oxygen species

1 Introduction

It is well established that oxidation and reduction (redox) reactions control biogeochemical processes and affect water quality in the environment (Kieber et al., 2003; Morel and Price, 2003; Learman et al., 2011). Early work provided the first theoretical evidence that the redox potential of seawater is controlled exclusively by the oxygen (O_2) system (Cooper, 1937). Since then, a great deal of work has generally confirmed that if present, the O_2 system has essential roles in controlling redox chemistry in the ocean (Keeling et al., 2009; Lu et al., 2018; Zhang et al., 2018). While the oxygen-water redox pair controls redox conditions over long-geological timescales, the situation is more complex, especially on timescales at which many biogeochemical processes occur (Rose, 2016). Along the four-electron pathway between oxygen and water are a set of reactive oxygen species (ROS), namely superoxide (O_2^-), hydrogen peroxide (H_2O_2) and hydroxyl radical ($OH^\bullet$), that individually participate in critical redox chemistry (Petasne and Zika, 1987; Sawyer, 1991; Wuttig et al., 2013; Sutherland et al., 2021), and ultimately have significant impacts on the biogeochemical cycling of essential trace elements and reduced carbon in the ocean (Zepp et al., 1992; Scully et al., 2003; White et al., 2003; Rose and Waite, 2006; Rose, 2016). The low seawater concentrations of these ROS (at fM to nM levels) reflect a balance of sources and sinks for each ROS in the system, revealing just how fast the redox cycle spins (Haag and Hoigne, 1986; Mopper and Zhou, 1990; Goldstone and Voelker, 2000).

In marine surface waters, photochemical reactions participate in redox chemistry by creating a diverse blend of oxidized and reduced chemical products (Andrews et al., 2000; Sharpless and Blough, 2014). The absorption of ultraviolet radiation (UVR; 290–400 nm) by chromophoric dissolved organic matter (CDOM) initiates photochemical reactions in the ocean (Mopper et al., 2015). Many of these photochemical reactions involve molecular oxygen, leading to the formation of an array of ROS, including those mentioned above (O_2^-, H_2O_2, and $OH^\bullet$) and singlet oxygen (Kieber et al., 2003; White et al., 2003; Rose and Waite, 2006; Kieber et al., 2014; Powers and Miller, 2015a; Ossola et al., 2021). The generation of these redox-active species is ubiquitous in sunlight-irradiated waters containing CDOM, with photochemical ROS production rates dependent on the solar photon flux, absorbance of solar energy, and photochemical reaction efficiency (Cooper and Zika, 1983; Kieber et al., 2014; Powers and Miller, 2014, 2016; Ossola et al., 2021).

In aquatic environments, H_2O_2 is important 1) in the degradation and indirect photobleaching of CDOM and organic pollutants (Goldstone et al., 2002; Scully et al., 2003), 2) in the redox cycling of biologically important trace metals (Moffett and Zika, 1987; Voelker and Sulzberger, 1996; Kieber et al., 2003; Miller et al., 2009), and 3) as an oxidative stress in aquatic ecosystems (Kieber et al., 2003; Zepp et al., 2003; Clark et al., 2008; Morris et al., 2011). H_2O_2 has been widely studied not only due to its biogeochemical reactivity, but also due to its greater concentration and stability relative to other ROS (O'Sullivan et al., 2005). However, it is O_2^- that represents the initial electron transfer to O_2 and subsequently serves as the photochemical precursor for H_2O_2. O_2^- is especially interesting because it can act as either an oxidant or a reductant, depending on the chemical encounter. If it reacts *via* an oxidative pathway it returns to the dissolved O_2 pool and again participates in oxidative reactions just like it always did. If it reacts *via* a reductive pathway, however, it can result in the production of H_2O_2, then $OH^\bullet$ and eventually water with a net "consumption" of O_2 (Sutherland et al., 2020). In this way, the production and reactive pathways for O_2^- in seawater serve as crucial controlling factors for many biological and chemical cycles in the photic zone (Rose, 2016).

There is good evidence for widespread dark extracellular O_2^- and H_2O_2 production by marine microorganisms (Diaz et al., 2013), confounding the long held idea that photochemistry is the primary marine source of O_2^-, and therefore, H_2O_2 in sunlit surface waters. A compilation of O_2^- production rates by marine cyanobacteria, phytoplankton, and heterotrophic bacteria suggests a marine biological oxygen sink amounting to 15–50% of the net oxygen production (Sutherland et al., 2020). Given that this estimate was not corrected for the much colder waters and slower biological rates in the deep dark ocean, as well as observations that H_2O_2 concentrations are negligible below the surface mixed layer, it is almost certainly an overestimate. However, the contribution of these known biological sources for ROS relative to abiotic photochemical production in sunlit surface waters remains unresolved. Furthermore, measured biological O_2^- rates are by definition "net" production rates and are typically determined in the absence of solar radiation (Diaz et al., 2013; Sutherland et al., 2020). It is currently unclear what, if any, changes in observed rates and pathways result from sunrise turning the nighttime into the day, with its myriad of UVR-generated chemical transients. While reduction (*via* catalase or peroxidase) is typically the dominant pathway for H_2O_2 decay, oxidation pathways have been reported to exceed reduction in some surface coastal waters, suggesting contribution of unknown abiotic or metabolic pathways (Sutherland et al., 2021). Photochemical O_2^- measurements may also be flawed, since they are often estimated using steady-state O_2^- concentrations in sunlit waters and dark decay rates (Powers et al., 2015). It is clear that decay rates in sunlit waters are not well defined and

quantitative data are sorely needed. Thus, our current understanding of these critical reactions required for accurate modeling of the redox state of the surface ocean remains incomplete.

Despite the uncertainties previously discussed, an evaluation of surface ocean photochemical O_2^- and H_2O_2 production rates based on the current state of the science is warranted. Powers and Miller (2014) presented a method to estimate global ocean photochemical H_2O_2 and O_2^- production using modeled solar irradiances and remotely sensed ocean color and temperature. However, depth-resolved rates were not calculated nor were error estimates presented. In this work, we improve upon this initial method in several ways. Notably the spectral efficiency of H_2O_2 photoproduction used in previous studies, represented by the apparent quantum yield (AQY) spectrum, was previously based on extended irradiations that likely resulted in an underestimate of AQY due to a lack of reciprocity (Powers and Miller, 2014). Here we update H_2O_2 photoproduction models using only AQY spectra determined when H_2O_2 accumulation rates are within a linear range (Kieber et al., 2014). Furthermore, Powers and Miller (2014) used a 2:1 stoichiometric ratio for O_2^-:H_2O_2 production based on an assumption that O_2^- dismutation adequately describes the relationship between O_2^- and H_2O_2 in open ocean seawater (Powers and Miller, 2014). Subsequently, direct, simultaneous measurements of O_2^- and H_2O_2 photoproduction rates for waters from deep profiles in the Gulf of Alaska revealed an average stoichiometry of 4:1, but with a large range between samples from the surface, 1,000 m, and just above the seafloor (Powers et al., 2015). Most relevant here, the ratio between O_2^- and H_2O_2 photoproduction rates for surface waters was highest, averaging 10.1 ± 5.4 or 13.8 ± 6.7 comparing rates normalized to CDOM absorbance (Powers et al., 2015). Work relating the photoproduction of one-electron reductants, the precursors for O_2^- and H_2O_2, also suggests that the ratio between O_2^- and H_2O_2 photoproduction is well above 2, ranging from 6—16 in a variety of natural and synthetic water samples (Zhang and Blough, 2016; Le Roux et al., 2021). These results are not surprising since the oxidation of O_2^- to O_2 is more thermodynamically favorable than reduction to H_2O_2 in conditions present in most surface waters (Sawyer, 1991; Rose, 2016).

Most importantly, photochemical rates in the surface ocean depend on the light available and the absorbance of that light by CDOM. Previous models of oceanic UV attenuation estimated from remotely sensed ocean color have assumed that the fraction of attenuation due to CDOM is 0.68 at 320 nm, a value determined by Fichot and Miller (2010) using a large open ocean data set. However, this average ratio must be extrapolated spectrally and can deviate greatly depending on dissolved water constituents and suspended particles (Cao et al., 2018; Zhu and Kieber, 2020). Algorithms that compute diffuse attenuation coefficients ($K_d(\lambda)$) (Fichot et al., 2008; Cao et al., 2014) and CDOM absorption coefficients ($a_g(\lambda)$) independently (Cao and Miller, 2015) allow for a more robust estimate of the light available for CDOM-initiated photochemical reactions in the surface ocean. This is especially true in complex inshore waters, where modeled photochemical rates can vary ± 100% between those that use this average $a_g(\lambda)/K_d(\lambda)$ ratio and those using $a_g(\lambda)$ and $K_d(\lambda)$ determined separately to calculate a specific ratio for each pixel (Cao et al., 2018). We previously assumed that these extreme differences in rates were not a problem for global ocean models (Powers and Miller, 2014), but $a_g(\lambda)/K_d(\lambda)$ for UV wavelengths can be much greater than 0.7 (Johannessen, 2003) and recent work demonstrated that modeled $a_g(\lambda)/K_d(\lambda)$ ratios exhibited a large range in the open ocean (Zhu and Kieber, 2020). These updates were used along with recent experimental data to provide new constraints on the magnitude of photochemical O_2^- and H_2O_2 production in the marine environment.

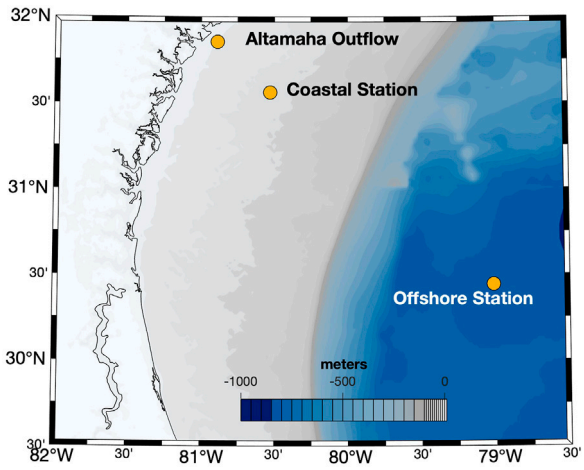

FIGURE 1
Locations of the sampling stations in the South Atlantic Bight. Bathymetry and topography data from the Global Self-consistent, Hierarchical, High-resolution Geography Database (GSHHG) were plotted using the m_map package for Matlab® (Pawlowicz, 2020). Water-column color coding indicates the depth in meters.

2 Materials and methods

2.1 Sample collection

Surface seawater (5 m) samples were collected at three stations in the South Atlantic Bight (SAB) aboard the R/V *Savannah* in March 2018. The geographic locations of the sampling stations are depicted in Figure 1. All samples were 0.2 μm gravity-filtered (Whatman Polycap 36AS) directly from Niskin bottles into combusted (4 h at 500°C) 1 L borosilicate glass bottles (Kimax). All tubing, filters, and bottle caps were

pre-cleaned with dilute (0.1 M) HCl and rinsed several times with 18.2 MΩ cm Milli-Q water (Millipore). Bottles were rinsed three times with filtered sample before final collection. Samples were irradiated within hours of collection, or within 1–2 days prior to an experiment. Samples not irradiated immediately after collection were stored at 4°C until use. Because many H_2O_2 photoproduction rates and AQY measurements have been made on stored samples (Kieber et al., 2014; Powers and Miller, 2014), shipboard irradiations were also conducted to determine H_2O_2 time-dependent photoproduction rates using freshly collected samples. These experiments were also used to assess how well modeled photoproduction rates predicted measured rates in freshly collected samples.

2.2 Laboratory H_2O_2 determination

H_2O_2 concentrations in seawater samples (including irradiated samples and dark controls) were measured with a flow injection analysis (FIA) chemiluminescence (CL) system (Waterville Analytical, FeLume) using methods described in detail previously (King et al., 2007; Powers et al., 2015). Briefly, the carrier solution (0.2 M HCl) and chemiluminescent reagent, 2 μM 10-methyl-9-(p-formylphenyl)acridinium carboxylate trifluoromethanesulfonate (AE), were mixed and pumped to a spiral flow cell (Global FIA) using a peristaltic pump (Rainin). A ~0.2 ml sample loop was filled by syringe and the sample was introduced to the carrier stream using a 10-port valve (VICI). The sample and carrier–AE solution mixed with 0.1 M carbonate buffer (pH 10.4) to initiate CL in the flow cell, which was situated below a photomultiplier tube (PMT; Hamamatsu HC135 PMT, 900 V, 400 ms integration). The PMT signal was recorded using Waterville Analytical software (LabView); 3—5 injections were repeated per sample. The FIA system was calibrated with H_2O_2 standards prepared in seawater using a 2 mM H_2O_2 stock solution diluted from 30% H_2O_2 (J.T. Baker), with concentrations confirmed using its absorbance at 240 nm and a molar absorptivity of 38.1 M^{-1} cm^{-1} (Miller and Kester, 1988).

2.3 Photochemical experiments

Photochemical experiments were conducted onboard the R/V *Savannah* with a Suntest CPS solar simulator (Atlas) equipped with a 1.5 kW Xenon lamp and a daylight filter to limit irradiation below 290 nm. These photochemical experiments were conducted to test for linearity in H_2O_2 photoproduction and to compare rates measured using freshly collected samples with those modeled as described in Sections 3.2, 3.4. Prior to irradiation, seawater samples were partitioned into 15 matched 10 cm cylindrical quartz spectrophotometric cells (Spectrocell) at room temperature. Cells were filled with no headspace and sealed using gas-tight screw caps with Teflon-faced butyl rubber septa. To ensure reproducible and quantifiable light exposures, cells were oriented vertically directly below the solar simulator in a black, anodized, water-cooled aluminum irradiation block. This block allowed no transfer of light between cells. The block was fitted with a half-inch thick grey PVC lid with 1.6 cm diameter holes centered directly above each cell window to remove residual off-axis photons and maximize collimated radiation within the cell, thus ensuring a reproducible and known pathlength for calculations (Powers and Miller, 2015b). The block was maintained at 20°C using a circulating water bath and cells were removed at various time points throughout each experiment to measure H_2O_2 and determine rates. One dark control was kept in the block and shielded from light while all other dark controls were kept in the water bath.

The spectral downwelling irradiance ($E_{0,lab}(\lambda)$; mol photons m^{-2} s^{-1} nm^{-1}) entering each cell was measured below the PVC lid for each cell position at 1 nm intervals with a UV-Vis portable spectroradiometer (OL756; Optronic Laboratories). The OL756, fitted with a quartz fiber optic cable and 2-inch diameter integrating sphere, was calibrated with a NIST standard lamp (OL752-10 irradiance standard; Optronic Laboratories) pre and post cruise. Under the irradiation conditions described above, the average integrated UV photon dose (290–400 nm) entering each cell was 33 W m^{-2} (~8.72 mol photons m^{-2} d^{-1}). The sample absorbance ($A(\lambda)$), before and after irradiation, was measured directly in each 10-cm cell using a single-beam UV-Vis spectrophotometer (Agilent). Milli-Q water was used as the absorbance blank and each $A(\lambda)$ sample spectrum was corrected for offsets or instrument drift by subtracting the average absorbance value in the 680–720 nm range. Corrected $A(\lambda)$ were converted to Naperian absorption coefficients ($a_{g,lab}(\lambda)$; m^{-1}) with the following equation:

$$a_{g,lab}(\lambda) = 2.303 \times A(\lambda) \Big/ L \tag{1}$$

where L is the cell pathlength (0.1 m). For these laboratory irradiations, H_2O_2 photoproduction rates ($P_{H_2O_2}(\lambda)$) were estimated using measured $a_{g,lab}(\lambda)$, $E_{0,lab}(\lambda)$, and the marine-average $\Phi_{H_2O_2,293K}(\lambda)$ with the following equation:

$$P_{H_2O_2}(\lambda) = E_{0,lab}(\lambda) \times S \times \Phi_{H_2O_2,293K}(\lambda) \times \left(1 - e^{-a_{g,lab}(\lambda) \times L}\right) \Big/ V \tag{2}$$

where S is the irradiated surface area (m^2) and V is the volume (m^3). $\Phi_{H_2O_2,293K}(\lambda)$ was calculated using Eqs. 5, 6 below. Simulated production rates were then determined by integrating Eq. 2 from 290—400 nm. The integrated photon dose ($Q_{a(int)}$) absorbed by CDOM from 290—400 nm for a given irradiation time interval was also calculated using Eq. 3.

$$Q_{a(int)} = \int_{290}^{400} E_{0,lab}(\lambda) \times S \times \left(1 - e^{-a_{g,lab}(\lambda) \times L}\right) d\lambda \tag{3}$$

2.4 Global photochemical model

In general, we followed the methods outlined in Fichot and Miller (2010) and Zhu and Kieber (2020) for global photochemical flux estimates. Briefly, H_2O_2 photochemical production rates ($P_{H_2O_2,z}$; mol m^{-3} d^{-1}) were estimated at each depth (z; m) with Eq. 4:

$$P_{H_2O_2,z} = \int_{290}^{400} \Phi_{H_2O_2,T}(\lambda) \times a_g(\lambda) \times E_{CL,0^-}(\lambda) \times e^{-K_d(\lambda)\times z} d\lambda \quad (4)$$

where $\Phi_T(\lambda)$ is the temperature-corrected AQY {[mol(mol photons)$^{-1}$]}, $a_g(\lambda)$ is the satellite-retrieved absorption coefficient of seawater (m^{-1}), $E_{CL,0^-}(\lambda)$ is the modeled, cloud-corrected, downwelling scalar irradiance immediately below the air-seawater interface (mol photons m^{-2} d^{-1} nm^{-1}), and $K_d(\lambda)$ is the satellite-retrieved diffuse attenuation coefficient for downwelling irradiance (m^{-1}). All global photochemical flux estimates reported in this work were conducted with a spectral resolution of 1 nm and a vertical depth (z) resolution of 0.1 m. We followed the procedure outlined in Zhu and Kieber (2020) to calculate $P_{H_2O_2,z}$ in the surface mixed layer, since the photochemical production integrated over this layer is expected to comprise 94–96% of all the photoproduction in the sunlit layer (Fichot and Miller, 2010). The mixed layer depth (MLD) data were obtained from the Monthly Isopycnal/Mixed-layer Ocean Climatology (https://www.pmel.noaa.gov/mimoc/, Schmidtko et al. (2013)).

We followed Zhu and Kieber (2020) and Cao et al. (2018) for the remote sensing retrievals of $a_g(\lambda)$ and $K_d(\lambda)$. Briefly, monthly climatologies of MODIS-Aqua reflectance ($R_{rs}(\lambda)$) from 2007 to 2017 were downloaded from the NASA Goddard Earth Sciences Data and Information Services Center (GES DISC, https://disc.gsfc.nasa.gov/). The monthly averaged $R_{rs}(\lambda)$ data, originally observed at MODIS wavebands (λ =412, 443, 469, 488, 531, 547, 555, 645, 667 and 678 nm), were linearly interpolated to SeaWiFs wavebands (λ =412, 443, 490, 510, 555, and 670 nm) prior to algorithm application. This was done to match Sea*CDOM* (Cao and Miller, 2015) and Sea*UV* (Fichot et al., 2008; Cao et al., 2014) algorithms that were subsequently used to retrieve $a_g(\lambda)$ and $K_d(\lambda)$, respectively. Note that this work used Sea*UV* with the updated parameters for offshore waters provided in Cao et al. (2014) to retrieve $K_d(\lambda)$ at 320, 340, 380, 412, 443, and 490 nm. To extend $K_d(\lambda)$ retrieved at six wavelengths to the full UV spectrum, K_d (320–400 nm) was determined with a cubic interpolation and K_d (290–319 nm) was calculated with a spectral slope coefficient determined between K_d (320 nm) and K_d (340 nm). The final data product of remote sensing retrievals of $a_g(\lambda)$ and $K_d(\lambda)$ were obtained with a wavelength resolution of 1 nm and a spatial resolution of 1° × 1°.

The SMARTS 2.9.5 model (Gueymard, 2001) was used to calculate monthly climatologies of the daily integrated spectral solar irradiance just above the sea surface under clear skies ($E_{0^+}(\lambda)$) from 2007 to 2017. Details regarding the computation of $E_{0^+}(\lambda)$, and the conversions from $E_{0^+}(\lambda)$ to clear-sky downwelling scalar irradiance immediately below the air-seawater interface $E_{clear,0^-}(\lambda)$ and from $E_{clear,0^-}(\lambda)$ to $E_{CL,0^-}(\lambda)$ are provided in Zhu and Kieber (2020). The loss of radiation at the air-seawater interface was calculated following the procedure outlined in Galí et al. (2016). A cloud correction factor (*CF*) was computed using the cloud-corrected and clear-sky UV spectral irradiance data at 308, 310, 324, and 380 nm, which were obtained from OMI/Aura Surface UVB Irradiance and Erythemal Dose dataset (downloaded from GES DISC). Details of the OMI UV products are provided by Tanskanen et al. (2006). Modeling $E_{0^+}(\lambda)$, $E_{clear,0^-}(\lambda)$, and $E_{CL,0^-}(\lambda)$ were performed with a wavelength resolution of 1 nm and a spatial resolution of 5 ° × 5 °. Cubic interpolation was applied to $E_{CL,0^-}(\lambda)$ to obtain a final data product with a spatial resolution of 1° × 1°.

For H_2O_2 photoproduction, Kieber et al. (2014) compared AQYs from a variety of seawater sources, including coastal and oligotrophic stations in Antarctica, the Pacific Ocean at Station ALOHA, the Gulf of Mexico, and several sites along the eastern coast of the United States. They found that AQYs exhibited limited variability for all regions studied when corrected for temperature. For our H_2O_2 photochemical production estimates, the following equation was used to estimate wavelength-dependent AQYs at 25°C:

$$\Phi_{H_2O_2,298K}(\lambda) = 1.70 \times e^{-0.0272\times\lambda} \quad (5)$$

The AQY spectrum in Eq. 5 was obtained from non-linear regression analyses of combined AQY data from all seawater sources studied by Kieber et al. (2014).

Temperature-dependent AQY ($\Phi_{H_2O_2,T}(\lambda)$) were calculated using an activation energy of 21.8 kJ mol^{-1}, as suggested by Kieber et al. (2014):

$$ln\frac{\Phi_{H_2O_2,T}(\lambda)}{\Phi_{H_2O_2,298K}(\lambda)} = \frac{21.8}{R}\left(\frac{1}{298} - \frac{1}{T}\right) \quad (6)$$

where R is the universal gas constant (8.314×10^{-3} kJ mol^{-1} K^{-1}) and T is the temperature (K). For our global estimate, $\Phi_{H_2O_2,T}(\lambda)$ appropriate for each pixel was adjusted using 11-year (2007–2017) averaged sea surface temperature (SST) using MODIS Aqua monthly datasets downloaded from GES DISC.

3 Results

3.1 H_2O_2 photoproduction in the South Atlantic Bight

H_2O_2 photoproduction rates were determined from the differences between H_2O_2 concentrations in irradiated seawater samples and dark controls. Changes in photoproduced [H_2O_2] were examined during prolonged irradiations of filtered seawater collected from three stations

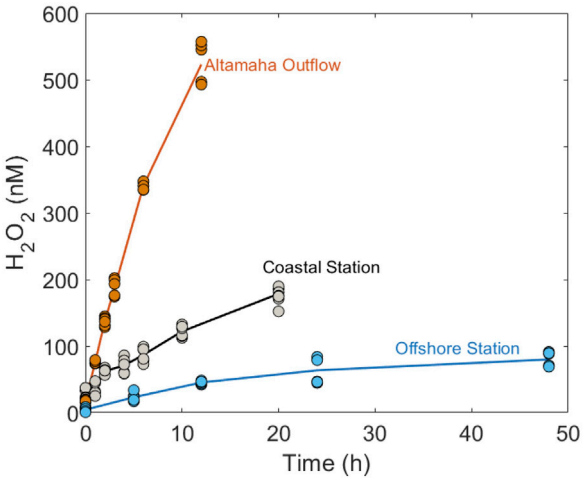

FIGURE 2
Photoproduced H_2O_2 versus irradiation time (h) for samples collected in the South Atlantic Bight in March 2018.

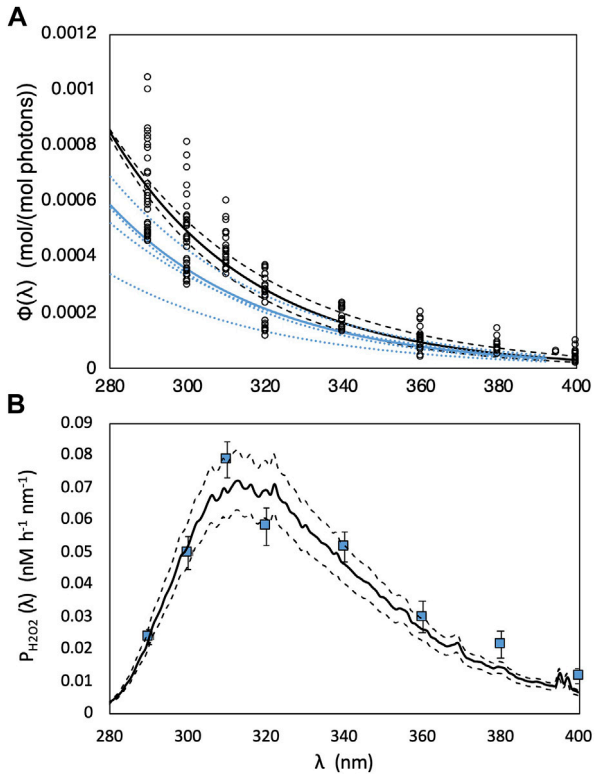

FIGURE 3
(A) "Marine-average" AQY spectrum [Φ(λ)] versus wavelength (λ; nm) (solid black line) computed from all measured monochromatic AQY data at 25°C reported in Kieber et al. (2014) (black open dots). Dashed black lines are the modeled AQY spectrum calculated using upper and lower limits of m_1 and m_2 in Table 1. The solid blue line shows pooled Φ(λ) computed from polychromatic AQY data reported in Powers and Miller (2016). Φ(λ) from individual experiments reported in Powers and Miller (2016) are depicted with blue dotted lines. **(B)** Simulated H_2O_2 photoproduction rates ($P_{H_2O_2}(\lambda)$) calculated for the Offshore Station using Eq. 2. The solid black line represents $P_{H_2O_2}(\lambda)$ estimated with the "marine-average" AQY spectrum, and the blue squares represent $P_{H_2O_2}(\lambda)$ calculated with average AQY values at each wavelength (error bars represent 95% CI). Dashed black lines represent $P_{H_2O_2}(\lambda)$ with ±13% error added.

in the SAB (Figure 2). These samples, designated as Altamaha Outflow, Coastal, and Offshore Stations provided a gradient from colored inshore to blue offshore water samples for the shipboard irradiations used to test our model's accuracy in different CDOM domains. These samples had average $a_{g,lab}$ (325 nm) values of 2.13, 0.56, and 0.22 m^{-1}, respectively. $Q_{a(int)}$ (Eq. 3) for the final time points were 90 µmol photons (12 h) for the Altamaha Outflow Station, 75 µmol photons (20 h) for the Coastal Station and 37 µmol photons (48 h) for the Offshore Station. However, H_2O_2 rates were no longer linear at these final timepoints, and therefore integrated photon doses calculated in this way do not have a simple, constant relationship to H_2O_2 photoproduction.

Previously, it was shown that the photoproduction of H_2O_2, as well as several other CDOM photoproducts (including CO, CO_2, and carbonyl compounds), is a nonlinear function of the light exposure time (Kieber et al., 2014; Powers and Miller, 2015b; Zhu and Kieber, 2018). Similarly, nonlinear accumulation was observed here for H_2O_2 photoproduction in seawater from the Altamaha Outflow, Coastal, and Offshore Stations (Figure 2), occurring at $Q_{a(int)}$ values of ~ 45, 12.5, and 9 µmol photons, respectively. Furthermore, H_2O_2 production rates calculated from a linear regression of [H_2O_2] with time, using all time points, were ~ 46%, 40%, and 65% lower, respectively, than H_2O_2 production rates determined before nonlinearity occurred. This result agrees with Kieber et al. (2014) who also reported a lack of reciprocity in H_2O_2 photoproduction during monochromatic irradiations (300–400 nm) of Gulf of Maine seawater. It should be noted here that nonlinearity cannot be accounted for by CDOM fading and that the photon dose at which nonlinear accumulation begins is sample dependent and should be tested prior to any AQY determination.

Under natural sunlight, the transition to non-linear H_2O_2 photoproduction should occur only after 1–2 days of exposure or more. This is because the daily downwelling solar irradiation in mid-latitude regions of NW Atlantic entering the ocean is ~ three times less than the daily-integrated irradiation output of the 1.5 kW Xenon lamp used in our shipboard irradiations. Furthermore, downwelling UV irradiance decreases exponentially with depth (Fichot and Miller, 2010; Zhu and Kieber, 2019). Depending on CDOM, MLD, and surface mixing rates, the average $Q_{a(int)}$ for any chromophore mixed through this varied radiation field is far smaller than the factor of

TABLE 1 Comparison between AQY parameters in Powers and Miller (2016) and the "marine-average" AQY parameters used in the global model. For monochromatic irradiations, AQY parameters were derived by a nonlinear regression of AQY versus λ. Uncertainties listed for m_1 and m_2 represent the margin of error with 95% confidence level. For polychromatic data, the parameters were determined using a non-linear curve-fitting routine in Matlab® (*nlinfit*), to solve for the best-fit equation to describe all light treatment data.

Station	m_1	m_2	Irradiation type	Reference
Marine-average	7.35 ± 0.049	0.0274 ± 0.0031	Monochromatic 25°C	Kieber et al. (2014)
SAB	7.70 ± 0.025	0.0254 ± 0.0049	Polychromatic 20°C	Powers and Miller (2016)
SAB	7.61	0.0254	Polychromatic adjusted to 25°C	this paper

three difference in initial $E_{CL,0^-}(\lambda)$ from simulated irradiation. This fact also argues that when extrapolating lab-determined photoproduction rates to surface ocean environments, AQYs determined from production rates over the initial linear range are most appropriate for accurate prediction. Consequently, the wavelength- and temperature-dependent AQYs used in our photochemical estimates were obtained using relatively short irradiation times (ca. 10–240 min depending on the seawater absorbance, the selected wavelength, and temperature; Kieber et al., 2014). The global photochemical estimates presented here (Sections 3.4, 3.5), using the updated AQY spectrum calculated from Eq. 5, are thus an improvement of the global AQY spectrum presented in Powers and Miller (2014), which used proper laboratory exposures but it was just that the time was wrong. In that work, irradiations lasted ~12 h, corresponding to 27 μmol photons absorbed under UV light treatments, which was well beyond the 9 μmol photon dose where nonlinearity was observed for the SAB Offshore Station (Figure 2).

3.2 Natural variability and errors associated with AQYs

For H_2O_2 photoproduction, a single "marine-average" AQY spectrum (Eq. 5) derived by Kieber et al. (2014) from a large variety of seawater sources, was used to model global photochemical production rates. As a limited test for its general applicability, we used this same average AQY to predict H_2O_2 production rates in our SAB samples. All wavelength-dependent AQY data reported by Kieber et al. (2014) and the "marine-average" AQY spectrum are shown in Figure 3A. The "marine-average" AQY spectrum is not statistically different from the AQY spectrum obtained using pooled AQY data in the Caribbean Sea, Orinoco River outflow (Venezuela), Suwanee River (Georgia, United States), Vineyard Sound (Massachusetts, United States), Shark River outflow (Florida, United States), and the Antarctic (Yocis et al., 2000). Here we also compare the "marine-average" AQY to the AQY spectra measured for the SAB by Powers and Miller (2016) (Figure 3A). For direct comparison with Powers and Miller (2016), the Kieber et al. (2014) "marine-average" AQY spectrum was fit to the following equation:

$$\Phi_{H_2O_2,298K}(\lambda) = e^{-(m_1+m_2(\lambda-290))} \quad (7)$$

where m_1 and m_2 are the fitting parameters obtained by fitting AQY data to Eq. 7. The fitting parameters with the 95% CI for AQY reported in Kieber et al. (2014) and Powers and Miller (2016) are presented in Table 1. As seen in Table 1, m_2 from the two studies are not significantly different, given the overlap in the 95% CI for m_2. A significant difference was observed for m_1 after a temperature correction (from 20°C to 25°C) was applied to the Powers and Miller (2016) AQY data. The difference in m_1 translates to a 23% difference in $\Phi_{H_2O_2,298K}$ at 290 nm. An underestimation in AQYs reported by Powers and Miller (2016) is expected given that the AQY spectra were determined from longer irradiations, which were likely beyond the initial linear range of $[H_2O_2]$ accumulation over time. Given that the difference in m_1 is smaller than the measurement uncertainties associated with the determination of wavelength-dependent AQYs (Table 2), the observed similarity in AQY spectra from different seawater sources with various optical properties gives us confidence that a single AQY equation (i.e., Eq. 5) can be used in our global photochemical model.

To assess the natural variability associated with wavelength-dependent AQYs, a summary of measured $\Phi_{H_2O_2,298K}(\lambda)$ at 290, 300, 320, 340, 360, and 400 nm (originally reported in Kieber et al., 2014) is presented in Table 2. The standard deviation in $\Phi_{H_2O_2,298K}(\lambda)$ increased with increasing wavelength, from 27% at 290 nm to 37% at 400 nm. There are more data points available in the UVB (290–320 nm) than at longer wavelengths, perhaps driving some of these increases. The Offshore Station in the SAB from the current study was used to examine how $P_{H_2O_2}(\lambda)$ (calculated from Eq. 2) varied as a function of wavelength (Figure 3B). The average AQYs at 290, 300, 320, 360, and 400 nm (Table 2) were used along with the average $E_{0,lab}(\lambda)$ and $a_{g,lab}(\lambda)$ at these wavelengths to calculate wavelength-dependent H_2O_2 photochemical production rates in the Offshore Station sample (data shown in blue squares, Figure 3B). The $P_{H_2O_2}(\lambda)$ calculated using the "marine-average" AQY is in reasonably good agreement with that calculated using wavelength-dependent AQY values reported in Kieber et al. (2014) with H_2O_2 photoproduction peaking at ~320 nm. Error (95% confidence level) in the "marine-average" AQY slope (i.e., m_2) is ~ ±11% (Table 1), resulting in a ±13%

TABLE 2 Summary of marine H_2O_2 Φ(λ) data [×10^{-4} mol/(mol photons)] determined at 25°C (Kieber et al., 2014) ± 1 SD, when available. ND is not determined.

Site	290 nm	300 nm	320 nm	360 nm	400 nm
Booth Bay Harbor, ME, United States	5.65 ± 0.33	4.10 ± 0.28	2.70 ± 0.31	1.19 ± 0.04	0.91 ± 0.09
Ammen Rock, Gulf of Maine, United States	6.49 ± 0.43	4.61 ± 0.08	2.64 ± 0.12	1.13 ± 0.04	0.54 ± 0.04
Rhode River Estuary, MD, United States	8.16 ± 0.32	5.27 ± 0.15	2.62 ± 0.21	1.03 ± 0.10	0.58 ± 0.03
Banks Channel, NC, United States	6.54 ± 0.40	5.27 ± 0.18	3.29 ± 0.33	1.06 ± 0.10	ND
Gulf of Mexico	8.08 ± 0.51	5.99 ± 0.31	3.61 ± 0.09	1.65 ± 0.43	0.32 ± 0.15
Station ALOHA	10.3 ± 0.23	7.35 ± 0.66	3.43 ± 0.15	1.59 ± 0.18	0.53 ± 0.04
Arthur Harbor, Palmer Station	4.83 ± 0.07	3.17 ± 0.13	1.40 ± 0.04	0.43 ± 0.01	0.30
Antarctic Station B	4.99 ± 0.13	3.30 ± 0.32	1.45 ± 0.12	0.74 ± 0.10	0.27 ± 0.11
Antarctic Station N	4.66 ± 0.11	3.49 ± 0.09	1.41 ± 0.31	0.71	0.21 ± 0.06
Average (*n*)	6.5 (33)	4.7 (34)	2.4 (31)	1.1 (22)	0.58 (16)
1 SD (CV)	1.8 (27%)	1.4 (29%)	0.85 (36%)	0.40 (37%)	0.21 (37%)

TABLE 3 Predicted H_2O_2 photoproduction rates in the quartz irradiation cells using the "marine-average" AQY and measured H_2O_2 photoproduction rates (± 1 SD) in filtered water samples at two time points. % differences between measured and predicted rates are also listed.

Station	Predicted in-cell rate (nM h^{-1})	Irradiation time (h)	Measured in-cell rate (nM h^{-1})	% Difference
Altamaha Outflow	39.5	2	59.8 ± 1.2	33
		6	53.5 ± 0.5	26
Coastal Station	10.2	4	11.5 ± 1.1	9.4
		10	9.3 ± 0.3	11
Offshore Station	4.3	5	3.7 ± 0.8	15
		12	3.4 ± 0.2	27

change in the integrated photoproduction rate from 290 to 400 nm. As seen in Table 2, the SD of measured AQYs at 320 nm is 36%, higher than the percentage differences between the predicted and measured rates as discussed below (Table 3). This measurement error likely drives most of the error in modeled photoproduction rates.

To further justify the use of the "marine-average" AQY in our global estimates, we compared measured H_2O_2 photoproduction rates in our SAB samples to those predicted using the "marine-average" AQY ($\Phi_{H_2O_2,293K}(\lambda)$) with measured $E_{0,lab}(\lambda)$ and $a_{g,lab}(\lambda)$ values from the short-term irradiations according to Eq. 2. Predicted production rates (calculated by integrating Eq. 2 from 290—400 nm) are presented in Table 3 along with measured rates and the % differences between the measured and predicted rates. All calculated production rates are in good agreement with measured rates (±9.4–27% in coastal to offshore water; Table 3). The biggest differences were observed for the Altamaha Outflow sample, and for samples that were exposed to prolonged irradiation with non-linear relationships between [H_2O_2] and photon exposure (e.g., the offshore sample exhibited a 15% error in predicted photoproduced H_2O_2 after 5 h versus 27% error in predicted photoproduced H_2O_2 after 12 h). Based on data shown in Table 3, we suggest that the "marine-average" AQY adequately represents the overall efficiency of H_2O_2 photoproduction in the SAB, with percentage differences between predicted and measured rates < 33%.

3.3 Errors associated with apparent quantum yield temperature adjustments using E_a

Natural variability was observed when fitting the Arrhenius equation to H_2O_2 data used to determine E_a (kJ mol^{-1}):

$$ln\,\Phi(\lambda) = ln\,A_p - \frac{E_a}{RT} \quad (8)$$

where A_p is a pre-exponential factor, R is the universal gas constant (8.314 × 10^{-3} kJ mol^{-1} K^{-1}), and T is temperature (K). The E_a and r^2 derived by fitting temperature-dependent AQYs in Kieber et al. (2014) to Eq. 8 are presented in Table 4. The resulting average E_a and 95% CI determined from the slope of Arrhenius equation (Eq. 8) for each wavelength is shown in

10.3389/frsen.2022.1009398

TABLE 4 E_a (kJ mol^{-1}) determined from the slope of the linear regression of ln [Φ(λ)] versus 1/T (K) and an R value of 8.315 × 10^{-3} kJ K^{-1} mol^{-1} at each wavelength as listed. Data were originally reported by Kieber et al. (2014). A pooled E_a was determined by a regression of all ln [Φ(λ)] versus 1/T data, regardless of wavelength. E_a at λ < 360 and λ ≥ 360 were also determined to assess the variability in E_a used in the global H_2O_2 model. Errors associated with E_a denote the margin of error with 95% confidence level.

Wavelength	E_a (kJ mol^{-1})	Percentage error	r^2 (n)
290 nm	16.1 ± 2.8	±17	0.60 (92)
300 nm	17.4 ± 3.3	±19	0.54 (94)
320 nm	19.5 ± 4.5	±23	0.47 (87)
360 nm	25.2 ± 9.4	±37	0.39 (48)
400 nm	24.6 ± 11	±46	0.32 (42)
Pooled	17.9 ± 5.7	±32	0.10 (363)
λ < 360	17.6 ± 3.5	±20	0.26 (273)
λ ≥ 360	23.8 ± 7.8	±33	0.30 (90)

Figure 4A, and the corresponding Arrhenius plot for all AQY data from 0—35°C (gray dots) reported in Kieber et al. (2014) are presented in Figure 4B. Based on a pooled linear regression (Figure 4B), overall error in $E_a(\lambda)$ was ±32%, but it was only ±20% when only wavelengths less than 360 nm were considered (Table 4). It should be noted that in laboratory irradiations, 82% (coastal water) to 86% (open ocean water) of the H_2O_2 photoproduction under UVR occurred at λ < 360 nm. Given this wavelength dependence, E_a used here is likely to generate errors closer to 20%. The reader should note that errors associated with E_a do not translate linearly to errors in AQY. For example, there was only a 5% difference in $\Phi_{H_2O_2,303K}$ when a 30% error in E_a was introduced into its 5°C adjustment from $\Phi_{H_2O_2,298K}$ using Eq. 6. Consequently, errors contained in using a single "marine average" AQY for model calculations are generally larger than any correction for temperature.

3.4 Modeled depth-dependent H_2O_2 photoproduction

Monthly climatologies of H_2O_2 photochemical production rates were determined at z = 0, 1, and 20 m using Eq. 4. Corresponding global maps of computed photoproduction rates are presented in Figure 5. We show global maps for February, May, August, and November, as representatives for the spatial variability of H_2O_2 photoproduction rates during each season. Global maps for $E_{CL,0^-}$ (320 nm), a_g (320 nm), K_d (320 nm), and SST in February, May, August, and November are presented in the Supplementary Material, Supplementary Figures S1–S4.

In surface waters, the spatial and vertical distribution of the modeled H_2O_2 photoproduction rate is similar to that observed

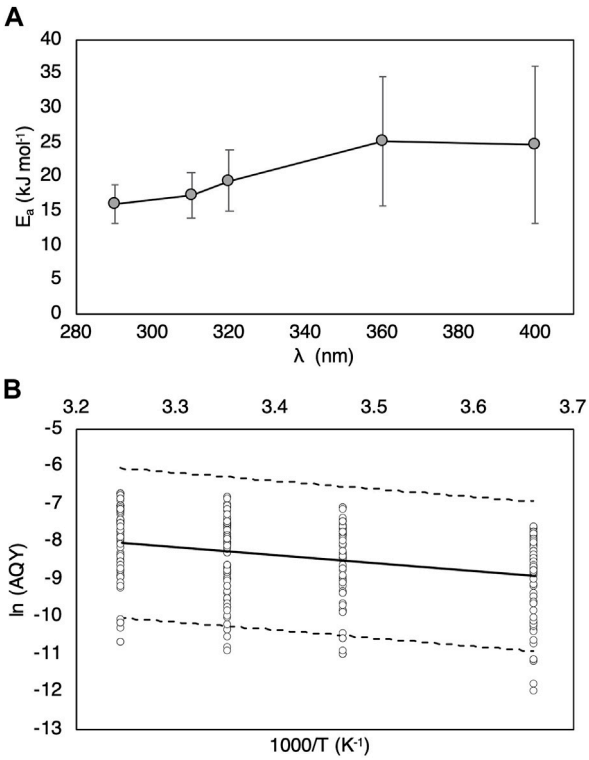

FIGURE 4
(A) Average activation energies (E_a) and 95% CI determined from the slope of the linear regression ln [Φ(λ)] versus 1/T (K^{-1}) for AQY data at each wavelength. **(B)** ln (AQY) versus 1,000/T (K^{-1}) (best-fit line is shown in solid black line; 95% prediction interval is bracketed by dashed lines) for all AQY data at from 0—35°C (gray dots) reported in Kieber et al. (2014).

for carbonyl compounds (Zhu and Kieber, 2020). In particular, the spatial distribution was mainly controlled by UV irradiance, the CDOM absorption coefficient and seawater temperature. High CDOM-absorbing coastal and upwelling areas exhibited the highest H_2O_2 photoproduction rates at 0 and 1 m (Figure 5). Equatorial waters also exhibited relatively high H_2O_2 photoproduction rates among open-ocean waters, due to their relatively high SST, upwelling in the equatorial eastern Pacific and the equatorial eastern Atlantic, as well as the high abundance of UV exposure. At mid-to high-latitudes, higher H_2O_2 photoproduction rates were found during the summer (e.g., August in the Northern Hemisphere) as compared to the winter (e.g., February in the Northern Hemisphere). The vertical distribution of H_2O_2 photoproduction rate in the water column was controlled by the exponential attenuation of UV radiation in the water column, resulting in H_2O_2 photoproduction rates at 20 m that were ~1–2 orders of magnitude lower than rates computed for the same location at 0 m. As expected, higher H_2O_2 photoproduction rates were calculated for oligotrophic waters at 20 m compared to coastal

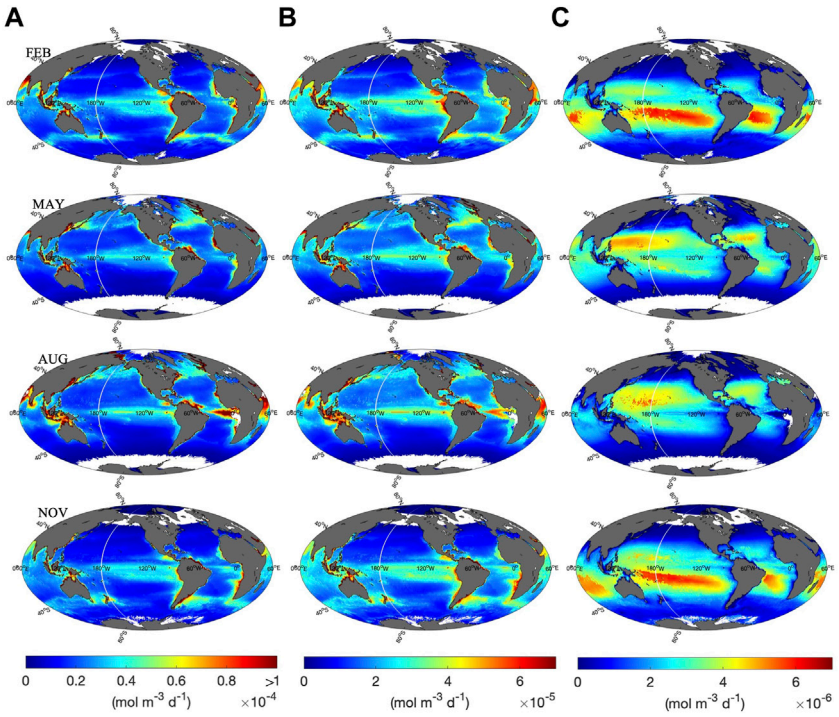

FIGURE 5
Calculated H_2O_2 photoproduction rates at **(A)** 0 m, **(B)** 1 m, and **(C)** 20 m in February, May, August and November. Note the difference in scale between **(A–C)**. White indicates no data.

and upwelling regions, due to deeper penetration of UV radiation compared to high CDOM-absorbing waters (Supplementary Figure S3).

Monthly 11-year (2007–2017) averaged estimates of H_2O_2 photoproduction rates at 0 m (computed with Eq. 4) are compared to previous literature reports of *in situ* H_2O_2 photoproduction rates to further evaluate our global model. Here we focus on low CDOM-absorbing waters in the open ocean that cover the majority of the surface area of the global oceans. Kieber et al. (2014) reported a daily H_2O_2 photoproduction rate of 72 nM d^{-1} at an oligotrophic station near 40 °N 70 °W in July 1999. By comparison, our modeled H_2O_2 photoproduction rate at 0 m for this location was 64 nM d^{-1} in July, only a 12% difference between the measured and climatologically modeled rate using an average marine AQY. This is within the ±33% error previously determined comparing our measured and predicted H_2O_2 photoproduction rates (Section 3.2). In Antarctic waters, Yocis et al. (2000) reported 2.4–3.5 nM h^{-1} *in situ* photoproduction rates near 60° S 55° W in summer, which translates to ~24–35 nM d^{-1} assuming that the daily integrated photon flux equals ten times the hourly photon flux measured during the incubation experiment. Our modeled rate for this location is 17 nM d^{-1} in December and is ~29% lower than the measured range. At our Offshore Station (near 30° N 79° W) in the SAB, we measured a 3.7 nM h^{-1} H_2O_2 photoproduction rate in March using a solar simulator with an integrated photon flux of 0.36 mol photons m^{-2} h^{-1}. For this location, integrating $E_{CL,0^-}(\lambda)$ from 290 to 400 nm yielded an integrated photon flux of 3.2 mol photons m^{-2} d^{-1} in March. Adjusting our measured H_2O_2 hourly rate to the modeled daily photon flux results in a value of 32.9 nM d^{-1}, higher than the 22.4 nM d^{-1} rate we modeled for 0 m. Even when forcing this comparison between laboratory solar simulation (with spectra from an artificial light source) and a 11-year climatological estimate based on natural sunlight, the ~32% difference between the measured and modeled photoproduction is not so far away and within the ±36% error that is associated with the natural variability of AQYs at 320 nm (Table 2).

A reasonable agreement between modeled and measured H_2O_2 photoproduction rates was also reported by Powers and Miller, (2014). The estimated H_2O_2 photoproduction rate at 1 m from this previous modeling effort was 63 nM d^{-1} at 40 °N 70 °W in July, and 32.5 nM d^{-1} at 55° S 55° W in December. In the present study, our modeled H_2O_2 photoproduction rates at 1 m isodepth are 49.4 nM d^{-1} at 40 °N 70 °W in July, and are 24.4 nM d^{-1} at 55° S 55° W in December. The ~30% difference between estimated photoproduction rates from the two models is

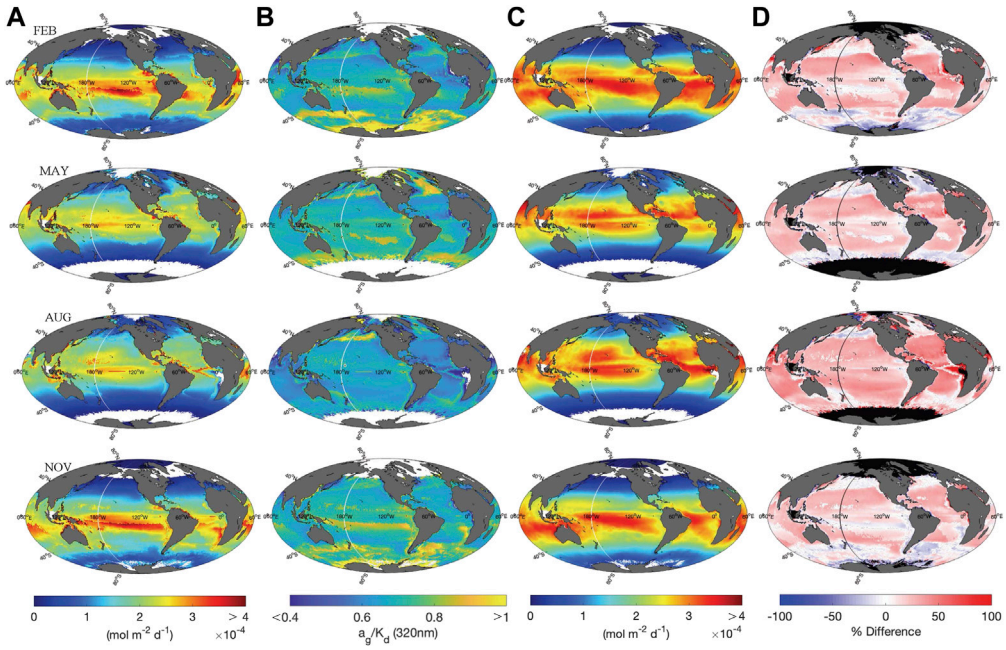

FIGURE 6
(A) Global maps of $P_{H_2O_2,integ}$, **(B)** a_g to K_d ratios at 320 nm, **(C)** $P'_{H_2O_2,integ}$ **(D)** the percentage difference between $P'_{H_2O_2,integ}$ and $P_{H_2O_2,integ}$ calculated from $\frac{P_{H_2O_2,integ}-P'_{H_2O_2,integ}}{P_{H_2O_2,integ}} \times 100$. Data in February, May, August and November are displayed. White color in panel **(A–C)** and black color in panel **(D)** indicates no data.

within the ±36% error that is associated with the natural variability of AQYs at 320 nm (Table 2).

3.5 Depth-integrated H_2O_2 photoproduction fluxes

Global maps depicting depth-integrated H_2O_2 photoproduction fluxes in the surface mixed layer ($P_{H_2O_2,integ}$) were calculated by integrating $P_{H_2O_2,z}$ (Eq. 4) from the ocean surface to the bottom of the surface mixed layer. Monthly climatologies for February, May, August, and November were used as representatives for each season in Figure 6. In the water column, ~96% of UV radiation is absorbed by CDOM in the surface mixed layer (Fichot and Miller, 2010) with an exponential decrease in UV intensity with depth in this layer; this is the most important factor affecting the geographical distribution of $P_{H_2O_2,integ}$. Thus, CDOM is the main driver for H_2O_2 photoproduction in our model, which is not surprising since it is inherent in the very concept of AQY used in this, and essentially all other environmental photochemical studies of natural processes. Given that the AQY is experimentally defined as the molar ratio of product (H_2O_2) and photons absorbed (CDOM), the partitioning of UV radiation between CDOM absorption and attenuation by other factors is the critical element in defining photochemical processes with AQY spectra. While there is a potential contribution of H_2O_2 photoproduction from the particulate phase, we have no data to support this so it is neglected in our model. The good agreement between CDOM modeled and measured *in situ* photochemical rates argues that, at least for H_2O_2, omitting particulate photoproduction is acceptable. Therefore, the a_g to K_d ratio (i.e., the ratio between CDOM absorption and total light attenuation) is the critical optical relationship needed to predict global patterns in $P_{H_2O_2,integ}$. As seen in Figure 6A, the highest $P_{H_2O_2,integ}$ are found in equatorial waters, as these waters receive a high abundance of UV radiation (Supplementary Figure S1) and exhibit relatively high a_g to K_d ratios (Figure 6B) and SST (Supplementary Figure S4).

To directly compare our photochemical model with several previous studies that used a constant a_g to K_d ratio in their global photoproduction models, we applied this same approach to estimate depth-integrated H_2O_2 photoproduction ($P'_{H_2O_2,integ}$) in sunlit waters without the capacity to adjust a_g/K_d based on ocean color data as follows:

$$P'_{H_2O_2,integ} = \iint_{290}^{400} \Phi_{H_2O_2,T}(\lambda) \times a'_g(\lambda) \times E_{CL,0^-}(\lambda) \times e^{-K'_d(\lambda)\times z} d\lambda dz \quad (9)$$

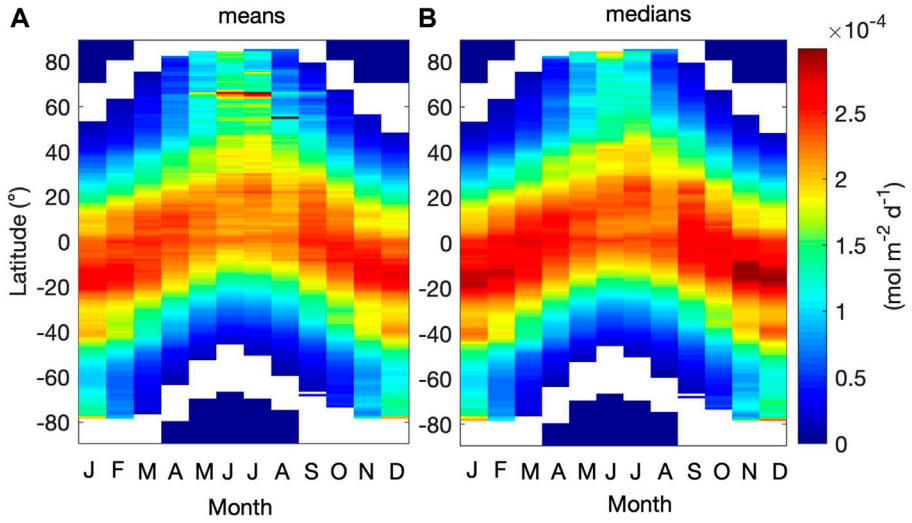

FIGURE 7
Hövemoller diagrams comparing the monthly **(A)** average and **(B)** median values of $P_{H_2O_2,integ}$ in 1° latitude bins. White color indicates no data.

TABLE 5 Estimated monthly and annually integrated H_2O_2 photoproduction budgets ($\Psi_{H_2O_2}$; $\Psi'_{H_2O_2}$). $\Psi_{H_2O_2}$ and $\Psi'_{H_2O_2}$ were calculated with $P_{H_2O_2,integ}$ and $P'_{H_2O_2,integ}$, respectively.

	Jan	Feb	Mar	Apr	May	Jun	Jul	Aug	Sep	Oct	Nov	Dec	Annual
	$\times 10^{12}$ mol month^{-1}												$\times 10^{13}$ mol year^{-1}
$\Psi_{H_2O_2}$	1.95	1.77	1.88	1.70	1.64	1.52	1.61	1.62	1.77	1.87	1.86	1.96	2.11
$\Psi'_{H_2O_2}$	2.16	2.00	2.17	1.95	1.85	1.71	1.82	2.02	2.01	2.13	2.04	2.11	2.40

where $a'_g(\lambda)$ was computed following Fichot and Miller (2010) using the original SeaUV algorithm (Fichot et al., 2008) to estimate $K'_d(\lambda)$, a constant a_g to K_d ratio of 0.68 at 320 nm, and an assumed exponential function: $a'_g(\lambda) = a'_g(320) \times e^{-S_{a_g} \times (\lambda - 320)}$ (S_{a_g} = 0.0194) to derive a CDOM spectrum for photochemical production. Although depth-integrated photochemical production rates were not calculated in Powers in Miller (2014), the same $a'_g(\lambda)$ calculation was applied in that earlier work. Our calculated $P'_{H_2O_2,integ}$ in February, May, August, and November are displayed in the global maps in Figure 6C. The percentage difference between $P_{H_2O_2,integ}$ and $P'_{H_2O_2,integ}$ are mapped in Figure 6D. $P'_{H_2O_2,integ}$ were significantly higher than $P_{H_2O_2,integ}$ in coastal and upwelling regions, which represent relatively low a_g/K_d (marked with deep blue in Figure 6B). We also found that regions with a_g/K_d (320 nm) > 0.8 (marked with yellow in Figure 6B) exhibited lower values of $P'_{H_2O_2,integ}$ compared to $P_{H_2O_2,integ}$ (Figure 6D). In open ocean areas where a_g/K_d (320 nm) was close to 0.68 (i.e., the assumed ratio used to calculate $a'_g(320)$), $P'_{H_2O_2,integ}$ was only slightly higher than $P_{H_2O_2,integ}$. The assumed S_{a_g} of 0.0194 may have contributed to overestimation of $P'_{H_2O_2,integ}$ in open-ocean areas, since this ratio was determined by pooling S_{a_g} data from a large variety of seawater sources including CDOM-rich, productive seawaters and oligotrophic waters. S_{a_g} has been shown to vary spatially and seasonally using ocean color data (Cao and Miller, 2015), consistent with photochemical fading of CDOM and seasonal riverine discharge. In oligotrophic waters, $a'_g(\lambda)$ is overestimated if S_{a_g} is higher than 0.0194 and a_g/K_d (320 nm) is close to 0.68.

Hövemoller diagrams depicting average and median monthly variations of $P_{H_2O_2,integ}$ are plotted in Figure 7 in 1° latitude bins. Seasonal variations in H_2O_2 photoproduction budgets in the surface mixed layer are also represented as monthly and annually integrated budgets ($\Psi_{H_2O_2}$) listed in Table 5. To obtain monthly integrated budgets, $P_{H_2O_2,integ}$ in each pixel was multiplied by the surface area (m^2) of the corresponding 1° × 1° block and the number of days in each month, and then summed. As shown in Figure 7 and Table 5, the summer months (e.g., July in

the Northern Hemisphere) exhibited the highest photoproduction budget and the winter season (e.g., July in the Southern Hemisphere) exhibited the lowest photoproduction budget. The annual H_2O_2 photoproduction budget was calculated as the sum of the monthly budgets, and an annual photoproduction budget of 21.1 Tmol yr^{-1} was obtained in this work. For comparison with Powers and Miller (2014), we also calculated monthly and annually integrated budgets ($\Psi'_{H_2O_2}$with $P'_{H_2O_2,integ}$ (data listed in Table 5). On average, the current study lowers the monthly H_2O_2 photoproduction budget estimate by 14% as compared to the modelling approach used in Powers and Miller, (2014).

For our annual H_2O_2 photoproduction budget estimate, errors contributed by uncertainties in model inputs were evaluated following the approach used by previous global photochemical models (Fichot and Miller, 2010; Zhu and Kieber, 2020). As discussed in Section 3.2, wavelength-dependent AQYs exhibited natural variability and we expect that the errors associated with the wavelength- and temperature-dependent AQYs are within 33% and 32%, respectively. In our global model, pooled fitting parameters for the "marine-average" AQY equation and an average value of E_a were used as model inputs. For wavelength-dependent AQY, the fitting parameters (m_1 and m_2) and the 95% CI are listed in Table 1; the 95% CI for m_1 and m_2 ranged from 7.30 to 7.40 and 0.0243–0.0305 m^{-1}, respectively. Using this range of model inputs for m_1 and m_2, corresponding global H_2O_2 photoproduction varied from 18.1 to 24.7 Tmol yr^{-1} and output uncertainties contributed by the pooled m_1 and m_2 values were <17%. For E_a, an average ± SD of 21.8 ± 8.2 kJ mol^{-1} was calculated from the activation energy data (λ = 300–360 nm) reported in Kieber et al. (2014). When E_a was varied from 13.6 to 30 kJ mol^{-1}, the global model resulted in H_2O_2 photoproduction values ranging between 20.8 and 21.6 Tmol yr^{-1}, demonstrating that uncertainties contributed by using an average E_a value were < 2%. We also performed a sensitivity analysis by adding 30% random noise to $\Phi_{H_2O_2,T}$, $E_{clear,0^-}$, CF, a_g, K_d and E_a. Readers are referred to Zhu and Kieber (2020) for a detailed description of the statistical approach used to evaluate the dependence of our global model outputs on errors associated with input parameters. Similar to Zhu and Kieber (2020) for carbonyl compounds, we estimate about a 37% uncertainty in predicted mixed-layer H_2O_2 photoproduction budgets. This translates to an uncertainty of 7.5 Tmol yr^{-1} in H_2O_2 photoproduction.

4 Discussion

4.1 Comparison of photochemical and biological H_2O_2 production

Results from this study can be used to compare photochemical and biological production of H_2O_2 in the marine environment. Palenik and Morel (1988) found evidence of a biological H_2O_2 source between 40 and 60 m in the Sargasso Sea, which they estimated to be on the order of 1–3 nM h^{-1}. Subsequent work in the Gulf of Alaska near Kodiak Island reported biological H_2O_2 production rates ranging from 1.1—1.9 nM h^{-1} in samples collected at 10 m based on H_2O_2-spiking experiments and modeling results (Vermilyea et al., 2010). Using a similar approach, Roe et al. (2016) found average biological H_2O_2 production rates at Station ALOHA to be 1.2 ± 0.9 nM h^{-1} at 25 m, 0.5 ± 0.2 nM h^{-1} at 75 m, and 0.1 ± 0.1 nM h^{-1} at the deep chlorophyll maximum, approximately 105–130 m. Intriguingly, biological O_2^- production rates were variable and generally lower in the same samples, amounting to 0.25 ± 0.14 nM h^{-1} at 25 m and 0.11 ± 0.25 at 75 m corresponding to the deep chlorophyll maximum (Roe et al., 2016). This implies that biologically produced H_2O_2 cannot result exclusively from extracellular dismutation. Recent work evaluated H_2O_2 production during incubations of 12 strains of representative marine bacteria and found a large range in rates from below detection to 300 amol $cell^{-1}$ h^{-1} (Bond et al., 2020). In comparing these rates to reported O_2^- production rates from the same bacteria, some species had rates of O_2^- and H_2O_2 that were comparable in magnitude, while others were different by orders of magnitude, again suggesting that the mechanisms whereby these two ROS are released to seawater may not be quantitively linked in biological systems and thus estimates that H_2O_2 is contributed to open ocean surface seawater at a rate of ~0.15 nM h^{-1} may be most reasonable (Bond et al., 2020).

If we consider a biological H_2O_2 production from 0.1—1 nM h^{-1} and a surface area of the ocean of 3.62 × 10^{14} m^2 (Charette and Smith, 2010), a very crude calculation of the biological production of H_2O_2 in the top 100 m yields an annual production of ~ 32–320 Tmol yr^{-1}. The lower end of this range is similar to our modeled H_2O_2 photoproduction estimate. However, this crudely calculated biological H_2O_2 production assumes a constant production rate determined from a limited number of ecological settings and species, so consequently, may vary significantly if evaluated for another time or another place. Global production estimates would likely decrease significantly if temperature dependence is considered, given that temperature typically decreases rates of biological activities (Crichton et al., 2021; Sarmento et al., 2010), e.g., by a factor of ~2 for every 10°C decrease in temperature (Packard et al., 1975). More work is needed to determine the effects of sunlight, temperature, and other stressors on the production of both O_2^- and H_2O_2 by marine microorganisms to refine this estimate.

4.2 Superoxide production budget estimate

To calculate the globally integrated O_2^- production budget we first estimated the O_2^-:H_2O_2 production ratio based on a survey of ratios described in the literature. Powers et al. (2015)

TABLE 6 Reported O_2^- and H_2O_2 photoproduction ratios and additional ancillary information.

Sample	O_2^-:H_2O_2 ratio	Method	Reference
Skidaway River Estuary, GA, United States	2.8	H_2O_2 measurements with and without added superoxide dismutase	Powers and Miller (2016)
Midshelf SAB	2.5		
Gulf Stream	3.4		
Gulf of Alaska surface water (n = 3)	2.4–10	Direct measurements in paired samples	Powers et al. (2015)
Gulf of Alaska average surface	10.1 ± 5.4	Average O_2^- rate divided by average H_2O_2 rate	

reported a ratio of 10.1(±5.4):1, determined from pooled photoproduction rates measured in marine surface water samples collected in the Gulf of Alaska. Interestingly, direct measurements of O_2^- and H_2O_2 at discrete time points over prolonged irradiation of the same samples yielded ratios with an even wider range from 2.4 to 10. The reader is referred to Table 6 for a summary of O_2^- and H_2O_2 photoproduction ratios in the SAB and the Gulf of Alaska (Powers et al., 2015; Powers and Miller, 2016). While those ratios do not represent initial rates required for photochemical rate modeling, much work remains to refine the quantitative relationship between photoproduced O_2^- and H_2O_2 in marine systems. Even though O_2^- photoproduction can be measured at pM s^{-1} levels, determining initial rates by linear regression of [O_2^-] versus time before steady-state concentrations are reached will likely underestimate true production since O_2^- decay is significant at all points in the time series. On the other hand, assumptions made to calculate O_2^- photoproduction from [O_2^-] steady-state values and measured dark decay rates may not accurately reflect the full suite of O_2^- reactions during solar radiation. Photoproduction rates of one-electron reductants (i.e., precursors for photoproduced O_2^-) suggest that O_2^- to H_2O_2 photoproduction ratios could range from 6 to 16 (Zhang et al., 2016; Le Roux et al., 2021), though open-ocean samples have not been tested. Le Roux et al. (2021) found ratios between one-electron reductants and O_2^- ranging from ~1.5 to 2 for standard reference materials. This was attributed to an inability to accurately determine O_2^- photoproduction rates. Recent work to model (Ma et al., 2020) and measure (Le Roux et al. in review; personal communication) light-dependent O_2^- decay has revealed that O_2^- estimates using steady-state concentrations and dark decay are in error, but again these experiments have not yet been conducted in seawater. Finally, the temperature dependence for O_2^- photoproduction is not known and has not been evaluated. Consequently, for our model assessment, we selected a O_2^-:H_2O_2 ratio of 10:1 as a reasonable value based on our current knowledge, allowing a back-of-the-envelope calculation of global O_2^- photochemical production on the order of ~211 Tmol yr^{-1}.

Direct measurements of particle-associated (i.e., biological) O_2^- production have been reported in several field studies. Rose et al. (2008) measured [O_2^-] in dark (30 min removed from sunlight) seawater downstream from particles collected on a 0.2 μm filter in the eastern equatorial Pacific, and reported O_2^- production of <1.1 nM h^{-1} at most depths but >1.8 nM h^{-1} at depths between 15 and 100 m. The maximum O_2^- production rate reported in Rose et al. (2008) was 4.4 nM h^{-1} at 30 m near the chlorophyll maximum at one station. In Great Barrier Reef lagoon waters, net, and presumably biological, O_2^- production rates were 18 ± 11 nM h^{-1} outside of a *Trichnodesnium* bloom and 25 ±14 nM h^{-1} inside the bloom (Rose et al., 2010). Similarly, net O_2^- production rates in samples from the Gulf of Alaska were <1– ~20 nM h^{-1} (Hansard et al., 2010) and were typically higher in the surface (~5–25 nM h^{-1}) than at 50 m (<1–7 nM h^{-1}). Thus, as an alternative estimate to that reported by Sutherland et al. (2020), we applied the same approach used above to estimate biological H_2O_2 production rates (See Section 4.1) and calculate biological O_2^- production in the top 100 m. Assuming that biological O_2^- production may be 1–20 nM h^{-1} and the surface area of the ocean is 3.62×10^{14} m^2 (Charette and Smith, 2010), annual O_2^- biological production could be on the order of 320–6,300 Tmol yr^{-1}. The lower end of the estimated range is of the same magnitude as our photochemical O_2^- flux estimate of ~211 Tmol yr^{-1} in the surface mixed layer. However, overestimation is expected regarding these biological O_2^- production estimates since, as in the H_2O_2 calculations, the temperature dependence of these rates was not quantified and thus were not considered.

4.3 Conclusion and implications

In this work, an annual H_2O_2 photoproduction budget of 21.1 ± 7.5 Tmol yr^{-1} was estimated using a global-scale photochemistry model driven by remotely sensed ocean data. This annual budget is significantly higher than global estimates for other marine photoproducts: carbon monoxide (2.5–4.2 Tmol yr^{-1}) (Zafiriou et al., 2003; Stubbins et al., 2006; Fichot and Miller, 2010), and the low-molecular-weight carbonyl compounds formaldehyde (4.1 Tmol yr^{-1}), acetaldehyde (2.0 Tmol yr^{-1}), glyoxal (0.35 Tmol yr^{-1}) and methylglyoxal (0.11 Tmol yr^{-1}) (Zhu and Kieber, 2020). It is often assumed that CO_2 is the dominant carbon-based photoproduct of CDOM photochemistry but rates supporting this contention were

primarily obtained from inshore waters (Miller and Zepp, 1995; Mopper and Kieber, 2002). Direct AQY measurements for open ocean seawater, however, are extremely limited. Previous estimates based on CO photochemical fluxes and a CO_2:CO ratio of 15 in riverine and coastal waters (Miller and Zepp, 1995), predict an annual CO_2 budget of 37.5–63 Tmol yr^{-1}. Our global modeled production for H_2O_2 seems to be of a similar magnitude as that for CO_2, suggesting that H_2O_2 is also a dominant photoproduct of marine photochemistry.

H_2O_2 photoproduction might serve as a better proxy than CO for estimating CO_2 photoproduction. Large variabilities were observed in CO_2:CO production ratios, greatly increasing the uncertainty of previous global estimates for CO_2 photoproduction that rely on this ratio (White et al., 2010; Reader and Miller, 2012). Powers and Miller (2015a) demonstrated that H_2O_2 and CO_2 photoproduction exhibited a well-defined relationship in a variety of marine waters and reported an average CO_2:H_2O_2 molar photoproduction ratio of 6.6 ± 1.8. Using an annual H_2O_2 photoproduction budget of 21.1 Tmol yr^{-1} and a CO_2: H_2O_2 molar ratio of 6.6, the estimated annual CO_2 photoproduction budget is 139 Tmol yr^{-1}, which is ~2–4 times higher than the CO_2 budget estimated with CO fluxes and a CO_2:CO ratio of 15. To further constrain the potential use of H_2O_2 as a proxy to estimate CO_2 photoproduction, much more work is needed to define the variability in CO_2: H_2O_2 ratios, particularly in blue water.

Our study provides constraints for O_2^- photoproduction in oceanic waters. Assuming a O_2^-: H_2O_2 production ratio of 10:1, gives an annual O_2^- photoproduction budget of ~211 Tmol yr^{-1}. Despite challenges and potentially large uncertainties with this estimate, attempts to quantify O_2^- photoproduction on a global scale are of great interest. The exact relationship between photochemical and biological production of O_2^- in marine environments may have important implications for oceanic redox chemistry and marine ecology. Sutherland et al. (2020), using a compilation of laboratory derived O_2^- production rates from marine microorganisms, estimated dark O_2^- production on the order of 3–4 Pmol yr^{-1} in the top 200 m, almost 20 times higher than our photochemical estimate in the surface mixed layer. It should be noted again that temperature and various other environmental stress factors (e.g., UV light) could significantly influence biological O_2^- production rates and these have yet to be evaluated. Consequently, it may be premature to extrapolate laboratory O_2^- dark production rates to large geographic scales.

In this work, we presented global-scale estimates of depth-resolved H_2O_2 photoproduction in sunlit surface seawater using remotely sensed ocean color. With slight modifications, the model employed in this study can be used to investigate ROS and other photo-redox reactions having defined AQY and temperature dependences at increasingly finer spatial and temporal resolutions. Our modeling approach provides new potential for examination of varying redox conditions and relationships to other important elemental cycles (e.g., Fe, Cu, Mn, N, C) in the surface oceans on regional scales and in relation to local transient oceanographic events (e.g., upwelling, rain, eddy evolution).

Data availability statement

The original contributions presented in the study are included in the article/Supplementary Material, further inquiries can be directed to the corresponding authors.

Author contributions

WM, LP, DK, and YZ designed the work. LP and WM conducted the sample collection and photochemistry experiments in the field. YZ ran the model. LP and YZ performed the data analyses. YZ, LP, DK, and WM prepared the manuscript.

Funding

Financial support was provided by the U.S. National Science Foundation through awards to the University of Georgia (OCE-1924763 and 1635618 to WM and LP) and SUNY-ESF (OCE-1756907 to DK).

Conflict of interest

The authors declare that the research was conducted in the absence of any commercial or financial relationships that could be construed as a potential conflict of interest.

Publisher's note

All claims expressed in this article are solely those of the authors and do not necessarily represent those of their affiliated organizations, or those of the publisher, the editors and the reviewers. Any product that may be evaluated in this article, or claim that may be made by its manufacturer, is not guaranteed or endorsed by the publisher.

Supplementary material

The Supplementary Material for this article can be found online at: https://www.frontiersin.org/articles/10.3389/frsen.2022.1009398/full#supplementary-material

References

Andrews, S. S., Caron, S., and Zafiriou, O. C. (2000). Photochemical oxygen consumption in marine waters: A major sink for colored dissolved organic matter? *Limnol. Oceanogr.* 45, 267–277. doi:10.4319/lo.2000.45.2.0267

Bond, R. J., Hansel, C. M., and Voelker, B. M. (2020). Heterotrophic bacteria exhibit a wide range of rates of extracellular production and decay of hydrogen peroxide. *Front. Mar. Sci.* 7, 00072. doi:10.3389/fmars.2020.00072

Cao, F., Fichot, C. G., Hooker, S. B., and Miller, W. L. (2014). Improved algorithms for accurate retrieval of UV/visible diffuse attenuation coefficients in optically complex, inshore waters. *Remote Sens. Environ.* 144, 11–27. doi:10.1016/J.RSE.2014.01.003

Cao, F., and Miller, W. L. (2015). A new algorithm to retrieve chromophoric dissolved organic matter (CDOM) absorption spectra in the UV from ocean color. *J. Geophys. Res. Oceans* 120, 496–516. doi:10.1002/2014JC010241

Cao, F., Mishra, D. R., Schalles, J. F., and Miller, W. L. (2018). Evaluating ultraviolet (UV) based photochemistry in optically complex coastal waters using the Hyperspectral Imager for the Coastal Ocean (HICO). *Estuar. Coast. Shelf Sci.* 215, 199–206. doi:10.1016/J.ECSS.2018.10.013

Charette, M. A., and Smith, W. H. F. (2010). The volume of Earth's ocean. *Oceanogr. Wash. D. C.* 23, 112–114. doi:10.5670/oceanog.2010.51

Clark, C. D., De Bruyn, W. J., Jakubowski, S. D., and Grant, S. B. (2008). Hydrogen peroxide production in marine bathing waters: Implications for fecal indicator bacteria mortality. *Mar. Pollut. Bull.* 56, 397–401. doi:10.1016/j.marpolbul.2007.10.017

Cooper, L. H. N. (1937). Oxidation-reduction potential in sea water. *J. Mar. Biol. Assoc. U. K.* 22, 167–176. doi:10.1017/s0025315400011929

Cooper, W. J., and Zika, R. G. (1983). Photochemical formation of hydrogen peroxide in surface and ground waters exposed to sunlight. *Science* 220, 711–712. doi:10.1126/science.220.4598.711

Crichton, K. A., Wilson, J. D., Ridgwell, A., and Pearson, P. N. (2021). Calibration of temperature-dependent ocean microbial processes in the cGENIE.muffin (v0.9.13) Earth system model. *Geosci. Model Dev.* 14, 125–149. doi:10.5194/gmd-14-125-2021

Diaz, J. M., Hansel, C. M., Voelker, B. M., Mendes, C. M., Andeer, P. F., and Zhang, T. (2013). Widespread production of extracellular superoxide by heterotrophic bacteria. *Science* 340, 1223–1226. doi:10.1126/science.1237331

Fichot, C. G., and Miller, W. L. (2010). An approach to quantify depth-resolved marine photochemical fluxes using remote sensing: Application to carbon monoxide (CO) photoproduction. *Remote Sens. Environ.* 114, 1363–1377. doi:10.1016/J.RSE.2010.01.019

Fichot, C. G., Sathyendranath, S., and Miller, W. L. (2008). Sea*UV* and SeaUV_C: Algorithms for the retrieval of UV/Visible diffuse attenuation coefficients from ocean color. *Remote Sens. Environ.* 112, 1584–1602. doi:10.1016/J.RSE.2007.08.009

Galí, M., Kieber, D. J., Romera-Castillo, C., Kinsey, J. D., Devred, E., Pérez, G. L., et al. (2016). CDOM sources and photobleaching control quantum yields for oceanic DMS photolysis. *Environ. Sci. Technol.* 50, 13361–13370. doi:10.1021/acs.est.6b04278

Goldstone, J. V., Pullin, M. J., Bertilsson, S., and Voelker, B. M. (2002). Reactions of hydroxyl radical with humic substances: Bleaching, mineralization, and production of bioavailable carbon substrates. *Environ. Sci. Technol.* 36, 364–372. doi:10.1021/es0109646

Goldstone, J. V., and Voelker, B. M. (2000). Chemistry of superoxide radical in seawater: CDOM associated sink of superoxide in coastal waters. *Environ. Sci. Technol.* 34, 1043–1048. doi:10.1021/es9905445

Gueymard, C. A. (2001). Parameterized transmittance model for direct beam and circumsolar spectral irradiance. *Sol. Energy* 71, 325–346. doi:10.1016/S0038-092X(01)00054-8

Haag, W. R., and Hoigne, J. (1986). Singlet oxygen in surface waters. 3. Photochemical formation and steady-state concentrations in various types of waters. *Environ. Sci. Technol.* 20, 341–348. doi:10.1021/es00146a005

Hansard, P. S., Vermilyea, A. W., and Voelker, B. M. (2010). Measurements of superoxide radical concentration and decay kinetics in the Gulf of Alaska. *Deep Sea Res. Part I Oceanogr. Res. Pap.* 57, 1111–1119. doi:10.1016/j.dsr.2010.05.007

Johannessen, S. C. (2003). Calculation of UV attenuation and colored dissolved organic matter absorption spectra from measurements of ocean color. *J. Geophys. Res.* 108, 3301. doi:10.1029/2000JC000514

Keeling, R. F., Körtzinger, A., and Gruber, N. (2009). Ocean deoxygenation in a warming world. *Ann. Rev. Mar. Sci.* 2, 199–229. doi:10.1146/annurev.marine.010908.163855

Kieber, D. J., Miller, G. W., Neale, P. J., and Mopper, K. (2014). Wavelength and temperature-dependent apparent quantum yields for photochemical formation of hydrogen peroxide in seawater. *Environ. Sci. Process. Impacts* 16, 777–791. doi:10.1039/C4EM00036F

Kieber, D. J., Peake, B. M., Neale, P. J., and Mopper, K. (2003). "Reactive oxygen species in aquatic ecosystems," in *UV effects in aquatic ecosystems*. Editors E. V. Helbling and H. Zagarese (Cambridge, UK: Royal Society of Chemistry), 251–288.

King, D. W., Cooper, W. J., Rusak, S. a., Peake, B. M., Kiddle, J. J., O'Sullivan, D. W., et al. (2007). Flow injection analysis of H_2O_2 in natural waters using acridinium ester chemiluminescence: Method development and optimization using a kinetic model. *Anal. Chem.* 79, 4169–4176. doi:10.1021/ac062228w

Le Roux, D. M., Powers, L. C., and Blough, N. V. (2021). Photoproduction rates of one-electron reductants by chromophoric dissolved organic matter via fluorescence spectroscopy: Comparison with superoxide and hydrogen peroxide rates. *Environ. Sci. Technol.* 55, 12095–12105. doi:10.1021/acs.est.1c04043

Learman, D. R., Voelker, B. M., Vazquez-Rodriguez, A. I., and Hansel, C. M. (2011). Formation of manganese oxides by bacterially generated superoxide. *Nat. Geosci.* 4, 95–98. doi:10.1038/ngeo1055

Lu, W., Ridgwell, A., Thomas, E., Hardisty, D. S., Luo, G., Algeo, T. J., et al. (2018). Late inception of a resiliently oxygenated upper ocean. *Science* 361, 174–177. doi:10.1126/science.aar5372

Ma, J., Nie, J., Zhou, H., Wang, H., Lian, L., Yan, S., et al. (2020). Kinetic consideration of photochemical formation and decay of superoxide radical in dissolved organic matter solutions. *Environ. Sci. Technol.* 54, 3199–3208. doi:10.1021/acs.est.9b06018

Miller, C. J., Rose, A. L., and Waite, T. D. (2009). Impact of natural organic matter on H_2O_2-mediated oxidation of Fe(II) in a simulated freshwater system. *Geochim. Cosmochim. Acta* 73, 2758–2768. doi:10.1016/j.gca.2009.02.027

Miller, W. L., and Kester, D. R. (1988). Hydrogen peroxide measurement in seawater by (p-Hydroxyphenyl)acetic acid dimerization. *Anal. Chem.* 60, 2711–2715. doi:10.1021/ac00175a014

Miller, W. L., and Zepp, R. G. (1995). Photochemical production of dissolved inorganic carbon from terrestrial organic matter: Significance to the oceanic organic carbon cycle. *Geophys. Res. Lett.* 22, 417–420. doi:10.1029/94GL03344

Moffett, J. W., and Zika, R. G. (1987). Reaction kinetics of hydrogen peroxide with copper and iron in seawater. *Environ. Sci. Technol.* 21, 804–810. doi:10.1021/es00162a012

Mopper, K., Kieber, D. J., and Stubbins, A. (2015). "Marine photochemistry of organic matter: Processes and impacts," in *Biogeochemistry of marine dissolved organic matter*. Editors D. A. Hansell and C. A. Carlson. 2nd Ed. (San Diego, CA: Academic Press), 389–450. doi:10.1016/B978-0-12-405940-5.00008-X

Mopper, K. W., and Kieber, D. J. (2002). "Chapter 9 – photochemistry and the cycling of carbon, sulfur, nitrogen and phosphorus," in *Biogeochemistry of marine dissolved organic matter*. Editors D. A. Hansell and C. A. Carlson (San Diego, CA: Academic Press), 455–507. doi:10.1016/B978-012323841-2/50011-7

Mopper, K., and Zhou, X. (1990). Hydroxyl radical photoproduction in the sea and its potential impact on marine processes. *Science* 250, 661–664. doi:10.1126/science.250.4981.661

Morel, F. M. M., and Price, N. M. (2003). The biogeochemical cycles of trace metals in the oceans. *Science* 300, 944–947. doi:10.1126/science.1083545

Morris, J. J., Johnson, Z. I., Szul, M. J., Keller, M., and Zinser, E. R. (2011). Dependence of the cyanobacterium prochlorococcus on hydrogen peroxide scavenging microbes for growth at the ocean's surface. *PLoS One* 6, e16805. doi:10.1371/journal.pone.0016805

Ossola, R., Jönsson, O. M., Moor, K., and McNeill, K. (2021). Singlet oxygen quantum yields in environmental waters. *Chem. Rev.* 121, 4100–4146. doi:10.1021/acs.chemrev.0c00781

O'Sullivan, D. W., Neale, P. J., Coffin, R. B., Boyd, T. J., and Osburn, C. L. (2005). Photochemical production of hydrogen peroxide and methylhydroperoxide in coastal waters. *Mar. Chem.* 97, 14–33. doi:10.1016/j.marchem.2005.04.003

Packard, T. T., Devol, A. H., and King, F. D. (1975). The effect of temperature on the respiratory electron transport system in marine plankton. *Deep Sea Res. Oceanogr. Abstr.* 22, 237–249. doi:10.1016/0011-7471(75)90029-7

Palenik, B., and Morel, F. M. M. (1988). Dark production of H_2O_2 in the Sargasso Sea. *Limnol. Oceanogr.* 33, 1606–1611. doi:10.4319/lo.1988.33.6part2.1606

Pawlowicz, R. (2020). *M_Map: A mapping package for MATLAB*. version 1.4m, [Computer software]. Available at: www.eoas.ubc.ca/~rich/map.html

Petasne, R. G., and Zika, R. G. (1987). Fate of superoxide in coastal sea water. *Nature* 325, 516–518. doi:10.1038/325516a0

Powers, L. C., Babcock-Adams, L. C., Enright, J. K., and Miller, W. L. (2015). Probing the photochemical reactivity of deep ocean refractory carbon (DORC): Lessons from hydrogen peroxide and superoxide kinetics. *Mar. Chem.* 177, 306–317. doi:10.1016/j.marchem.2015.06.005

Powers, L. C., and Miller, W. L. (2016). Apparent quantum efficiency spectra for superoxide photoproduction and its formation of hydrogen peroxide in natural waters. *Front. Mar. Sci.* 3, 00235. doi:10.3389/fmars.2016.00235

Powers, L. C., and Miller, W. L. (2014). Blending remote sensing data products to estimate photochemical production of hydrogen peroxide and superoxide in the surface ocean. *Environ. Sci. Process. Impacts* 16, 792–806. doi:10.1039/C3EM00617D

Powers, L. C., and Miller, W. L. (2015a). Hydrogen peroxide and superoxide photoproduction in diverse marine waters: A simple proxy for estimating direct CO_2 photochemical fluxes. *Geophys. Res. Lett.* 42, 7696–7704. doi:10.1002/2015GL065669

Powers, L. C., and Miller, W. L. (2015b). Photochemical production of CO and CO_2 in the Northern Gulf of Mexico: Estimates and challenges for quantifying the impact of photochemistry on carbon cycles. *Mar. Chem.* 171, 21–35. doi:10.1016/j.marchem.2015.02.004

Reader, H. E., and Miller, W. L. (2012). Variability of carbon monoxide and carbon dioxide apparent quantum yield spectra in three coastal estuaries of the South Atlantic Bight. *Biogeosciences* 9, 4279–4294. doi:10.5194/bg-9-4279-2012

Roe, K. L., Schneider, R. J., Hansel, C. M., and Voelker, B. M. (2016). Measurement of dark, particle-generated superoxide and hydrogen peroxide production and decay in the subtropical and temperate North Pacific Ocean. *Deep Sea Res. Part I Oceanogr. Res. Pap.* 107, 59–69. doi:10.1016/j.dsr.2015.10.012

Rose, A. L., Godrant, A., Godrant, A., Furnas, M., and Waite, T. D. (2010). Dynamics of nonphotochemical superoxide production in the Great Barrier Reef lagoon. *Limnol. Oceanogr.* 55, 1521–1536. doi:10.4319/lo.2010.55.4.1521

Rose, A. L. (2016). The influence of reactive oxygen species on local redox conditions in oxygenated natural waters. *Front. Earth Sci.* 4, 1–11. doi:10.3389/feart.2016.00096

Rose, A. L., and Waite, T. D. (2006). Role of superoxide in the photochemical reduction of iron in seawater. *Geochim. Cosmochim. Acta* 70, 3869–3882. doi:10.1016/j.gca.2006.06.008

Rose, A. L., Webb, E. A., Waite, T. D., and Moffett, J. W. (2008). Measurement and implications of nonphotochemically generated superoxide in the equatorial Pacific Ocean. *Environ. Sci. Technol.* 42, 2387–2393. doi:10.1021/es7024609

Sarmento, H., Montoya, J. M., Vázquez-Domínguez, E., Vaqué, D., and Gasol, J. M. (2010). Warming effects on marine microbial food web processes: How far can we go when it comes to predictions? *Philos. Trans. R. Soc. B Biol. Sci.* 365, 2137–2149. doi:10.1098/rstb.2010.0045

Sawyer, D. T. (1991). *Oxygen chemistry*. Oxford, United Kingdom: Oxford University Press.

Schmidtko, S., Johnson, G. C., and Lyman, J. M. (2013). Mimoc: A global monthly isopycnal upper-Ocean Climatology with mixed layers. *J. Geophys. Res. Oceans* 118, 1658–1672. doi:10.1002/jgrc.20122

Scully, N. M., Cooper, W. J., and Tranvik, L. J. (2003). Photochemical effects on microbial activity in natural waters: The interaction of reactive oxygen species and dissolved organic matter. *FEMS Microbiol. Ecol.* 46, 353–357. doi:10.1016/S0168-6496(03)00198-3

Sharpless, C. M., and Blough, N. V. (2014). The importance of charge-transfer interactions in determining chromophoric dissolved organic matter (CDOM) optical and photochemical properties. *Environ. Sci. Process. Impacts* 16, 654–671. doi:10.1039/C3EM00573A

Stubbins, A., Uher, G., Law, C. S., Mopper, K., Robinson, C., and Upstill-Goddard, R. C. (2006). Open-ocean carbon monoxide photoproduction. *Deep Sea Res. Part II Top. Stud. Oceanogr.* 53, 1695–1705. doi:10.1016/j.dsr2.2006.05.011

Sutherland, K. M., Grabb, K. C., Karolewski, J. S., Taenzer, L., Hansel, C. M., and Wankel, S. D. (2021). The redox fate of hydrogen peroxide in the marine water column. *Limnol. Oceanogr.* 66, 3828–3841. doi:10.1002/lno.11922

Sutherland, K. M., Wankel, S. D., and Hansel, C. M. (2020). Dark biological superoxide production as a significant flux and sink of marine dissolved oxygen. *Proc. Natl. Acad. Sci. U. S. A.* 117, 3433–3439. doi:10.1073/pnas.1912313117

Tanskanen, A., Krotkov, N. A., Herman, J. R., and Arola, A. (2006). Surface ultraviolet irradiance from OMI. *IEEE Trans. Geosci. Remote Sens.* 44, 1267–1271. doi:10.1109/TGRS.2005.862203

Vermilyea, A. W., Paul Hansard, S., and Voelker, B. M. (2010). Dark production of hydrogen peroxide in the Gulf of Alaska. *Limnol. Oceanogr.* 55, 580–588. doi:10.4319/lo.2010.55.2.0580

Voelker, B. M., and Sulzberger, B. (1996). Effects of fulvic acid on Fe(II) oxidation by hydrogen peroxide. *Environ. Sci. Technol.* 30, 1106–1114. doi:10.1021/es9502132

White, E. M., Kieber, D. J., Sherrard, J., Miller, W. L., and Mopper, K. (2010). Carbon dioxide and carbon monoxide photoproduction quantum yields in the Delaware Estuary. *Mar. Chem.* 118, 11–21. doi:10.1016/j.marchem.2009.10.001

White, E. M., Vaughan, P. P., and Zepp, R. G. (2003). Role of the photo-Fenton reaction in the production of hydroxyl radicals and photobleaching of colored dissolved organic matter in a coastal river of the southeastern United States. *Aquatic Sci. - Res. Across Boundaries* 65, 402–414. doi:10.1007/s00027-003-0675-4

Wuttig, K., Heller, M. I., and Croot, P. L. (2013). Pathways of superoxide (O_2^-) decay in the eastern tropical north atlantic. *Environ. Sci. Technol.* 47, 10249–10256. doi:10.1021/es401658t

Yocis, B. H., Kieber, D. J., and Mopper, K. (2000). Photochemical production of hydrogen peroxide in Antarctic Waters. *Deep Sea Res. Part I Oceanogr. Res. Pap.* 47, 1077–1099. doi:10.1016/S0967-0637(99)00095-3

Zafiriou, O. C., Andrews, S. S., and Wang, W. (2003). Concordant estimates of oceanic carbon monoxide source and sink processes in the Pacific yield a balanced global "blue-water" CO budget. *Glob. Biogeochem. Cycles* 17, 1015. doi:10.1029/2001GB001638

Zepp, R. G., Callaghan, T. V., and Erickson, D. J., III (2003). Interactive effects of ozone depletion and climate change on biogeochemical cycles. *Photochem. Photobiol. Sci.* 2, 51–61. doi:10.1039/B211154N

Zepp, R. G., Faust, B. C., and Hoigne, J. (1992). Hydroxyl radical formation in aqueous reactions (pH 3-8) of iron(II) with hydrogen peroxide: The photo-fenton reaction. *Environ. Sci. Technol.* 26, 313–319. doi:10.1021/es00026a011

Zhang, F., Xiao, S., Kendall, B., Romaniello, S. J., Cui, H., Meyer, M., et al. (2018). Extensive marine anoxia during the terminal Ediacaran Period. *Sci. Adv.* 4, eaan8983. doi:10.1126/sciadv.aan8983

Zhang, T., Diaz, J. M., Brighi, C., Parsons, R. J., McNally, S., Apprill, A., et al. (2016). Dark production of extracellular superoxide by the coral porites astreoides and representative symbionts. *Front. Mar. Sci.* 3, 00232. doi:10.3389/fmars.2016.00232

Zhang, Y., and Blough, N. V. (2016). Photoproduction of one-electron reducing intermediates by chromophoric dissolved organic matter (CDOM): Relation to O_2^- and H_2O_2 photoproduction and CDOM photooxidation. *Environ. Sci. Technol.* 50, 11008–11015. doi:10.1021/acs.est.6b02919

Zhu, Y., and Kieber, D. J. (2019). Concentrations and photochemistry of acetaldehyde, glyoxal and methylglyoxal in the Northwest Atlantic Ocean. *Environ. Sci. Technol.* 53, 9512–9521. doi:10.1021/acs.est.9b01631

Zhu, Y., and Kieber, D. J. (2020). Global model for depth-dependent carbonyl photochemical production rates in seawater. *Glob. Biogeochem. Cycles* 34, 1–20. doi:10.1029/2019GB006431

Zhu, Y., and Kieber, D. J. (2018). Wavelength and temperature-dependent apparent quantum yields for photochemical production of carbonyl compounds in the North Pacific Ocean. *Environ. Sci. Technol.* 52, 1929–1939. doi:10.1021/acs.est.7b05462